

# X-ray Microdiffraction Images of Antiferromagnetic Domain Evolution in Chromium

P. G. Evans,<sup>1\*</sup> E. D. Isaacs,<sup>1</sup> G. Aeppli,<sup>2</sup> Z. Cai,<sup>3</sup> B. Lai<sup>3</sup>

Magnetic x-ray diffraction combined with x-ray focusing optics was used to image individual antiferromagnetic spin density wave domains in a chromium single crystal at the micron scale. The cross section for nonresonant magnetic x-ray scattering depends on the antiferromagnetic modulation vector and spin polarization direction and allows these quantities to be extracted independently. The technique was used to show that the broadening of the nominally first-order "spin-flip" transition at 123 kelvin, at which the spins rotate by 90°, originates at the walls between domains with orthogonal modulation vectors. During cooling, the transition begins at these walls and progresses inward. The modulation vector domains are themselves unchanged.

The antiferromagnetic ordering of elemental chromium was postulated in 1936 by Louis Néel but had to await the invention of neutron diffraction for confirmation (1). Body-centered cubic Cr is the quintessential example of a structurally simple metal exhibiting complex magnetism. Electron spins in this material order in a long-period density wave, and on cooling not only undergo a transition between a disordered paramagnetic phase and an ordered Néel state, at the Néel transition temperature ( $T_N$ ), but also display a transition between Néel states of mutually perpendicular spin polarizations, at  $T_{SF}$  (SF, "spin-flip"). Although this latter spin-flip transition dominates many physical properties of Cr below room temperature, the mechanism and dynamics of the nucleation and growth of antiferromagnetic domains remain elusive, because no suitable microscopies have combined sensitivity to antiferromagnetism and spatial resolution (2, 3). We describe here a magnetic x-ray diffraction technique exploiting focusing optics to visualize antiferromagnetic domains at the micron scale. As an example of this technique, we show that the spin-flip transition begins at the walls between domains with orthogonal propagation directions for the spin modulation and coarsens inward.

Coulomb interactions among electrons and the geometry of the Fermi surface within which electrons reside conspire (4–6) to produce the spin density wave (SDW) in Cr below the Néel transition at 311 K. The SDW has an amplitude, or peak magnetic moment,

of 0.6 bohr magneton per atom and a modulation vector that can lie along any of the three  $\langle 001 \rangle$  axes of the Cr crystal lattice

(7). The transition we are interested in is not the Néel transition but the spin-flip transition near  $T_{SF} = 123$  K, where the SDW changes between transverse and longitudinal polarization states (Fig. 1A). One signature of the spin-flip transition occurs in the bulk magnetic susceptibility, which undergoes a small step at the critical temperature (Fig. 1B). Although magnetic susceptibility data allow the identification of anomalies, they do not by themselves provide explanations for them. The most useful tools in this respect are magnetic neutron and x-ray diffraction, in which scattering arises from electron spins in the same way as from atomic cores in conventional neutron and x-ray diffraction. Data are collected in reciprocal rather than direct space and contain sharp Bragg peaks derived from coherent spin density modulations. For Cr, with lattice constant  $a$ , the period  $Da$  of the spin modulation is incommensurate with the Cr lattice. The ordered magnetic state leads to new Bragg reflections at distances  $\delta = 1/D \approx 0.05$  in reciprocal space from the

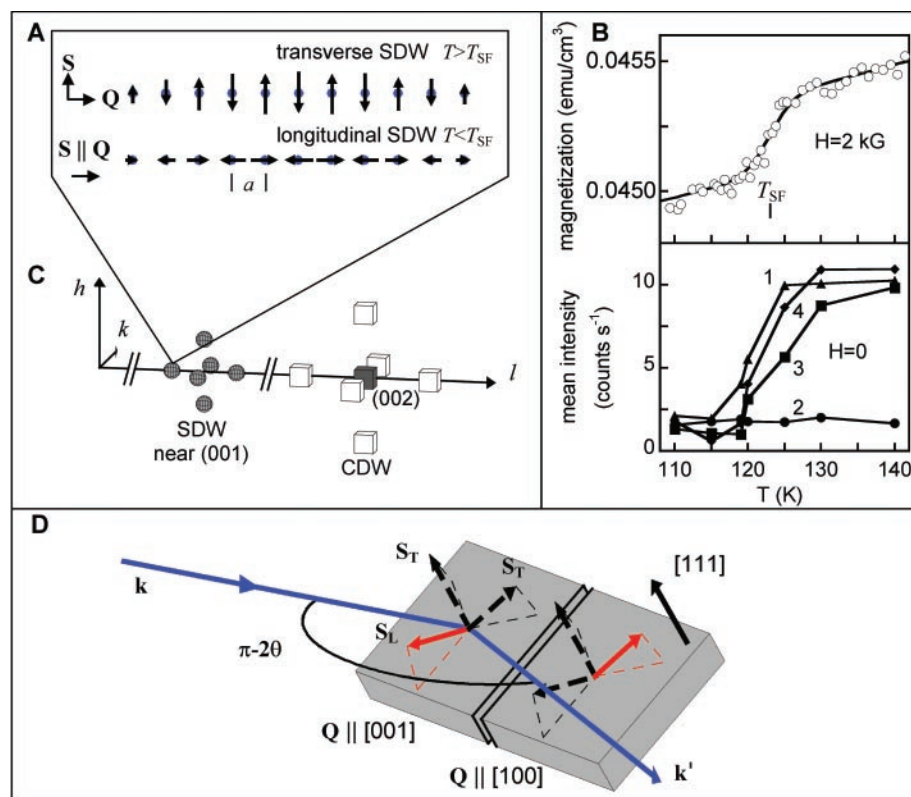


**Fig. 1.** (A) At  $T_{SF}$ , the spin polarization  $S$  changes from transverse to longitudinal with respect to the modulation wave vector  $Q$ . The period of the spin modulation is incommensurate with the lattice spacing  $a$ . (B) (Upper panel) A step in the bulk magnetization of Cr in an applied field of 2 kG serves as a marker for the spin-flip transition. (Lower panel) The mean intensity in the numbered areas of Fig. 3 plotted as a function of temperature demonstrates that  $T_{SF}$  varies by more than 7 K across this single SDW domain. (C) The positions of the (002) allowed Bragg reflection (solid cube), CDW satellite (open cubes), and SDW satellite (spheres) peaks are shown in regions of reciprocal space near (001) and (002). (D) The incident and diffracted beams  $k$  and  $k'$  for a  $Q \parallel [001]$  domain near a  $Q$  domain wall. Transverse-polarized spins in this domain (dashed lines, labeled  $S_T$ ) have components that are not in the diffraction plane and thus result in more intense scattering than spins polarized along  $Q$  (solid line, labeled  $S_L$ ). Ordered spins in the neighboring domain with  $Q \parallel [100]$  result in no diffracted intensity, because the Bragg diffraction condition is not satisfied.

<sup>1</sup>Bell Laboratories, Lucent Technologies, 600-700 Mountain Avenue, Murray Hill, NJ 07974, USA. <sup>2</sup>NEC Research Institute, 4 Independence Way, Princeton, NJ 08540, USA. <sup>3</sup>Advanced Photon Source, Argonne National Laboratory, 9700 South Cass Avenue, Argonne, IL 60439, USA.

\*To whom correspondence should be addressed. E-mail: pevans2@lucent.com

points  $(h, k, l)$ , where  $h+k+l$  is odd, at which Bragg peaks due to atomic cores are forbidden for the body-centered cubic structure (8, 9). The SDW also induces modulations in the charge and lattice that are proportional to the square of the SDW; this follows because the coupling between charge and spin is invariant with respect to spin reversal, allowing only even powers of the spin to couple to charge. The resulting charge density wave (CDW) then has half the period of the SDW, leading to additional nonmagnetic Bragg peaks displaced by  $2\delta$  from the  $(h, k, l)$  points with even  $h+k+l$  (10). The locations of SDW and CDW reflections near (001) and (002) in reciprocal space are shown (Fig. 1C).

For ferromagnets, magnetic domains are characterized by a single parameter: the spin polarization. For antiferromagnetic Cr, two parameters are needed: the spin polarization  $\mathbf{S}$  and modulation wave vector  $\mathbf{Q}$ , which can be independently determined by x-ray diffraction using the magnetic scattering reflection arising directly from the SDW and the conventional Thomson scattering from the CDW (9). To spatially resolve  $\mathbf{S}$  and  $\mathbf{Q}$ , magnetic x-ray microscopy experiments were performed at a hard x-ray microprobe facility at the Advanced Photon Source of Argonne National Laboratory. The source of synchrotron radiation was an undulator insertion device with the photon energy selected by a two-crystal Si (111) monochromator. The x-ray microprobe beam was produced by means of a Fresnel zone plate followed by a 20- $\mu\text{m}$  aperture in a Pt-Ir disk passing only radiation focused to the first-order spot (11, 12). This focusing technique has only recently been made possible by the development of high-brilliance synchrotron x-ray sources. The  $(0, 0, 1-\delta)$  SDW reflection was measured with a probe spot size of 0.5  $\mu\text{m}$ , using 5.8-keV incident photons. This photon energy is be-

low the 5.95-keV threshold for exciting Cr K shell characteristic fluorescence, eliminating a source of background. To study the  $(0, 0, 2-2\delta)$  CDW reflection at nearly the same diffractometer angles, the photon energy was tuned to 11.6 keV. The maximum count rates from the SDW and CDW reflections were 10 and 2500 counts per second, respectively.

The scattering plane for our diffraction experiments, defined by the wave vectors  $\mathbf{k}$  and  $\mathbf{k}'$  of the incident and diffracted beams, was normal to the [110] direction, so that the momentum transfer  $\mathbf{k}'-\mathbf{k}$  was along [001] (Fig. 1D). Previous studies of Cr crystals have found that SDW domains with a component of  $\mathbf{Q}$  along the surface normal are preferentially occupied in the near-surface region because of strain effects (9, 13). In order to ensure a diversity of SDW domain orientations, our experiments were performed with a polished Cr (111) single crystal (purchased from Alfa Aesar, Ward Hill, MA), in which we observed all three possible orientations of  $\mathbf{Q}$  using CDW reflections in rotating anode x-ray diffraction experiments.

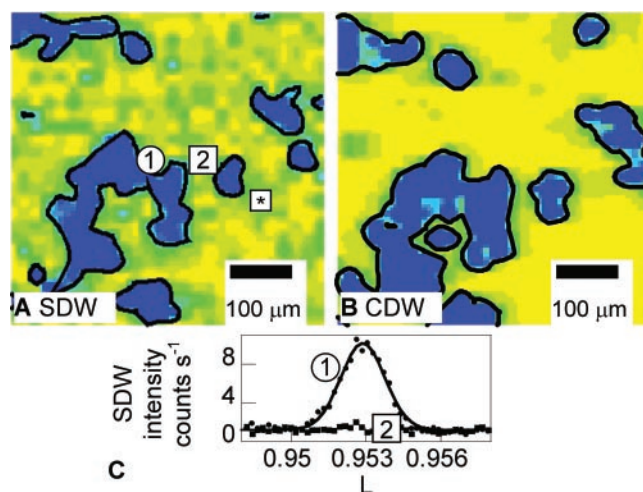
Images of individual domains of  $\mathbf{Q}$  were formed by measuring the intensity of either the SDW or CDW reflection as a function of the position of the sample under the beam. The equivalence in our geometry of the two reflections as a means of observing  $\mathbf{Q}$  domains at temperatures above  $T_{\text{SF}}$  will be demonstrated below. An image of the  $(0, 0, 1-\delta)$  SDW intensity, collected with a 20- $\mu\text{m}$  step size at 130 K, is shown (Fig. 2A). Scanning the same area with the  $(0, 0, 2-2\delta)$  CDW reflection reveals a nearly identical domain structure (Fig. 2B), in which the areas of higher intensity enclosed by black lines correspond to regions in which the propagation wave vector  $\mathbf{Q}$  is along [001]. The roughly 20- $\mu\text{m}$  absorption length for both 5.8- and 11.6-keV x-rays leads to significant contri-

butions to the diffracted signal from depths of up to several microns. The characteristic length scale of the domains ranges from tens to hundreds of microns. In contrast to the domain patterns typical of ferromagnets, the domains of  $\mathbf{Q}$  are highly irregular in shape and size, suggesting that relatively weak random imperfections dictate the domain geometry.

The intensity map of the SDW reflection can be understood in the context of the dependence of the magnetic x-ray scattering cross section on the spin polarization  $\mathbf{S}$  and the directions  $\hat{\mathbf{k}}$  and  $\hat{\mathbf{k}}'$  of the incident and diffracted beams. Two spin terms contribute to the nonresonant cross section for scattering, which is proportional to  $|\mathbf{S} \cdot (\hat{\mathbf{k}} \times \hat{\mathbf{k}}')|^2 + |\mathbf{S} \cdot \hat{\mathbf{k}}(1 - \hat{\mathbf{k}} \cdot \hat{\mathbf{k}}')|^2$  (14). With our diffraction conditions, the first term dominates when  $\mathbf{S}$  is not in the scattering plane. Because the sample was mounted with [110] normal to the diffraction plane, the magnetic scattering cross sections for the two possible transverse spin polarizations were equal. In the areas of intense scattering in Fig. 2A, the SDW domains thus have  $\mathbf{Q}$  along [001] and  $\mathbf{S}$  perpendicular to  $\mathbf{Q}$ . Spins oriented in the scattering plane (with  $\mathbf{S}$  along the [001] direction; i.e., in the longitudinal SDW phase below  $T_{\text{SF}}$ ) have a magnetic scattering cross section resulting only from the second term above, which is reduced by a factor of 30 in comparison with the cross section for spins along perpendicular directions. Scans along  $(0, 0, l)$  in reciprocal space taken at points on and off an area of intense scattering (Fig. 2C) illustrate that the contrast in Fig. 2A arises from the SDW domains and not simply from the variation of the position of the SDW peak in reciprocal space across the sample.

We have exploited the dependence of the magnetic scattering cross section on  $\mathbf{S}$  to study the spin-flip transition in detail. The intensity of magnetic scattering from domains in which  $\mathbf{Q}$  is in the scattering plane is drastically decreased upon cooling through  $T_{\text{SF}}$ . This effect has been previously observed in x-ray experiments, but without spatial resolution (9). Selection rules applicable to neutron scattering can lead to a similar decrease in the scattered neutron intensity below  $T_{\text{SF}}$  (8). The SDW domain marked with a star is shown in images made with a 3- $\mu\text{m}$  step size (Fig. 3).<sup>13</sup> As the sample was cooled through the spin-flip transition in a series of steps from 140 to 110 K, the region in which scattering was observed decreased in extent and disappeared as the spins reoriented to point along  $\mathbf{Q}$ . During each measurement, the sample reached a steady-state temperature that was held for several hours; these can thus be considered maps of the magnetic domains in thermal equilibrium. Comparison of the image at 130 K with one taken at that temperature upon warming (not shown) reveals

**Fig. 2.** Magnetic domains in Cr at  $T = 130$  K. Maps of the intensity of the (A) SDW reflection at  $(0, 0, 1-\delta)$  and (B) CDW reflection at  $(0, 0, 2-2\delta)$  in a region 500  $\mu\text{m}$  by 500  $\mu\text{m}$  are shown. These images (including those in Figs. 3 and 4) have been resampled on a grid with four times the point density of the original scan and smoothed with a three-pixel-square moving average. The intensity scale for these images ranges from yellow (lowest count rate) to blue (highest count rate). The saturation level and threshold



for the domain outlines are chosen to emphasize the domain contrast and are scaled between the two images by the ratio of the mean count rate. (C) Reciprocal space scans along  $(0, 0, l)$  at the positions indicated on the SDW map. The solid line is a Gaussian fit to the scan at position 1.

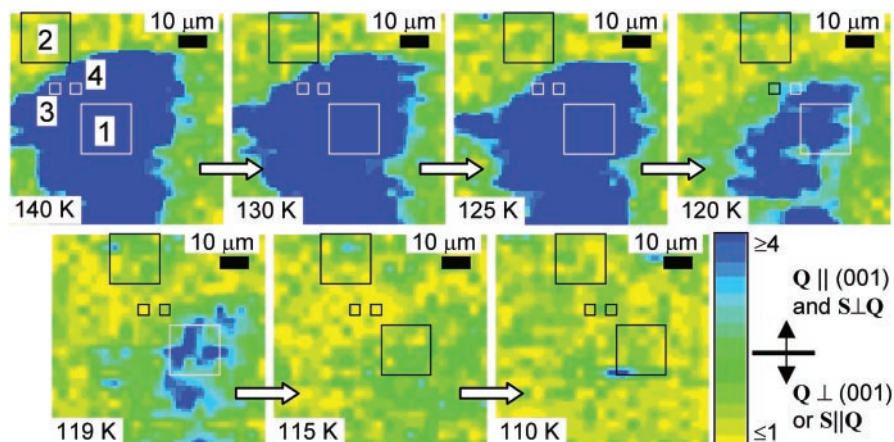


**Fig. 3.** Images of a single SDW domain at temperatures near  $T_{SF}$ . This domain also appears at a different scale in Fig. 2A, where it is marked with an asterisk. The transition from transverse to longitudinal spin polarization at  $T_{SF}$  results in the disappearance of magnetic scattering from the SDW domain. The numbered boxes refer to regions over which the intensities were averaged to yield the temperature dependences plotted in Fig. 1B.

that thermal hysteresis is negligible on the micron scale. In contrast to the SDW, images made at 130 and 110 K using the CDW reflection from the same domain (Fig. 4) illustrate that scattering from the CDW is the same above and below  $T_{SF}$ . The extent of the  $\mathbf{Q} \parallel [001]$  domain is thus unchanged by the spin-flip transition. The dramatic drop in the intensity of magnetic scattering observed in Fig. 3 can be attributed solely to the reorientation of the spins below  $T_{SF}$  from transverse to longitudinal upon cooling.

Because the spin-flip transition is first order, with a well-known latent heat and change in volume (7), it can be expected to take place at a single temperature in a homogeneous system. The fact that different points in the images of Fig. 3 are converted from blue to yellow-green at different temperatures shows that this is not the case for our Cr sample. The variation in transition temperature across the  $\mathbf{Q} \parallel [001]$  domain is illustrated by Fig. 1B, in which the mean intensity in four regions of the images of Fig. 3 is plotted as a function of temperature and set against the magnetization jump, which is the bulk signature of the spin-flip transition. At each temperature, the positions of the region of integration were adjusted to compensate for linear shifts in the position of the beam on the sample due to contraction of the sample holder upon cooling. Although points 3 and 4 are only 5  $\mu\text{m}$  apart,  $T_{SF}$  at the two points differs by 5 K. The count rate in area 1, where  $T_{SF}$  is lowest, remains constant as the spin-flip transition occurs at points 3 and 4, falling only at a lower temperature. The mean intensity in area 2, a region in which  $\mathbf{Q}$  is perpendicular to  $[001]$  and there are neither  $(0,0,1-\delta)$  SDW nor  $(0,0,2-2\delta)$  CDW peaks, is unchanged on passing through  $T_{SF}$ .

A phase transition broadened by impurities or other defects is common enough: The defects nucleate the low-temperature phase, which then grows into the regions occupied by the high-temperature phase (15). A recent example of this is the growth of ferromagnetism starting at natural and artificial grain boundaries in manganite films (16). What we have discovered here is the nucleation of a magnetic phase not at a structural grain boundary, as for the manganite films, but at its magnetic equivalent. Indeed, the combination of our x-ray charge (Fig. 4) and spin (Fig. 3) images of magnetic domains in Cr clearly show that the spin-flip transition begins at the boundary between  $\mathbf{Q}$  domains, across which there is a  $90^\circ$  rotation of  $\mathbf{Q}$ , and progresses inward.

There are three microscopic effects that could be responsible for our discoveries. The first is somewhat similar to what occurs for exchange biasing, a crucial concept underlying useful magnetoresistive devices (17), which is based on a local moment model that considers only short-range exchange interactions, as for an insulator. The key insights are that one of the transverse spin directions on one side of a  $90^\circ$   $\mathbf{Q}$  domain wall actually points along the longitudinal direction on the other side, and that a Heisenberg exchange interaction would favor antiparallel rather than perpendicular alignment. Inevitably, because of disorder, one of the transverse domains will be more stable than the other, allowing it, via the exchange interaction, to nucleate the longitudinal state in the less stable transverse domain. Another mechanism, very much analogous to what is suspected for the manganite films (16), invokes strain fields, which may be either the cause or the effect of the  $\mathbf{Q}$  domain walls. The idea here is that  $T_{SF}$  is a strong function of strain (18, 19), and that near the  $\mathbf{Q}$  domain walls the strain is sufficient to raise  $T_{SF}$  by the observed

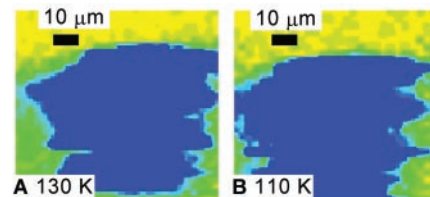


**Fig. 4.** Images of the CDW reflection intensity in the area of Fig. 3 at (A) 130 K and (B) 110 K. The  $\mathbf{Q}$  orientation and size of the SDW domain are unchanged by cooling through  $T_{SF}$ .

amount. The final and in many respects most interesting candidate mechanism invokes the quantum mixing of states with different Fermi surfaces across the domain wall. The mixing will result in a different spin-orbit coupling near that interface, which could then stabilize the longitudinal phase at a higher temperature.

The magnetic x-ray microscope images described here are an important first step toward understanding the relationship of microscopic domains to the bulk properties of this common element and prototypical magnet. The interplay between macroscopically observable phenomena and the configuration of domains and domain walls, both magnetic and ferroelectric, is becoming increasingly important as density requirements in many technologies drive device feature sizes toward those of individual domains. Recent achievements of multilayer magnetic devices with antiferromagnetic coupling layers have stimulated a renewed interest in Cr and other antiferromagnetic materials (20–22). Our experiments are important beyond the world of Cr, because the ability to image antiferromagnetic domains with the same ease with which magnetic force microscopy can image ferromagnetic domains is a prerequisite for the scientifically based engineering of antiferromagnets.

#### References and Notes

1. C. G. Shull, M. K. Wilkinson, *Rev. Mod. Phys.* **25**, 100 (1953).
2. M. Ando, S. Hosoya, *Phys. Rev. Lett.* **29**, 281 (1972).
3. J. B. Davidson, S. A. Werner, A. S. Arrot, *Magnetism and Magnetic Materials*, AIP Conference Proceedings No. 18, C. D. Graham Jr., J. J. Rhyne, Eds. (American Institute of Physics, New York, 1973), part I, pp. 396–400.
4. A. W. Overhauser, *Phys. Rev.* **128**, 1437 (1962).
5. W. M. Lomer, *Proc. Phys. Soc. (London)* **80**, 489 (1962).
6. T. M. Rice, *Phys. Rev. B* **2**, 3619 (1970).
7. E. Fawcett, *Rev. Mod. Phys.* **60**, 209 (1988).
8. S. A. Werner, A. Arrot, H. Kendrick, *Phys. Rev.* **155**, 528 (1967).
9. J. P. Hill, G. Helgesen, D. Gibbs, *Phys. Rev. B* **51**, 10336 (1995).
10. M. Mori, Y. Tsunoda, *J. Phys. Condens. Matter* **5**, L77 (1993).
11. B. Lai *et al.*, *Appl. Phys. Lett.* **61**, 1877 (1992).
12. E. Di Fabrizio *et al.*, *Nature* **401**, 895 (1999).
13. K.-F. Braun, S. Fölsch, G. Meyer, K.-H. Rieder, *Phys. Rev. Lett.* **85**, 3500 (2000).
14. M. Blume, D. Gibbs, *Phys. Rev. B* **37**, 1779 (1988).
15. Y. Imry, M. Wortis, *Phys. Rev. B* **19**, 3580 (1979).

16. Y.-A. Soh, G. Aeppli, N. D. Mathur, M. G. Blamire, *Phys. Rev. B* **63**, 020402 (2001).  
 17. J. Nogués, I. K. Schuller, *J. Magn. Mater.* **192**, 203 (1999).  
 18. J. E. Mattson, S. D. Bader, M. B. Brodsky, J. B. Ketterson, *J. Magn. Mater.* **109**, 179 (1992).  
 19. H. Zabel, *J. Phys. Condens. Matter* **11**, 9303 (1999).  
 20. M. N. Baibich *et al.*, *Phys. Rev. Lett.* **61**, 2472 (1988).  
 21. A. Scholl *et al.*, *Science* **287**, 1014 (2000).  
 22. F. Nolting *et al.*, *Nature* **405**, 767 (2000).  
 23. Use of the Advanced Photon Source was supported

by the U.S. Department of Energy, Office of Science, Office of Basic Energy Sciences, under contract no. W-31-109-Eng-38. The authors thank R. Pindak and G. Blumberg for helpful discussions.

5 October 2001; accepted 8 January 2002

# Magnetic Resonant Mode in the Single-Layer High-Temperature Superconductor $\text{Tl}_2\text{Ba}_2\text{CuO}_{6+\delta}$

H. He,<sup>1</sup> P. Bourges,<sup>2</sup> Y. Sidis,<sup>2</sup> C. Ulrich,<sup>1</sup> L. P. Regnault,<sup>3</sup> S. Pailhès,<sup>2</sup> N. S. Berzigiariova,<sup>4</sup> N. N. Kolesnikov,<sup>4</sup> B. Keimer<sup>1\*</sup>

An unusual spin excitation mode observed by neutron scattering has inspired numerous theoretical studies of the interplay between charged quasiparticles and collective spin excitations in the copper oxide high-temperature superconductors. The mode has, thus far, only been observed in materials with crystal structures consisting of copper oxide bilayers, and it is absent in the single-layer compound  $\text{La}_{2-x}\text{Sr}_x\text{CuO}_{4+\delta}$ . Neutron-scattering data now show that the mode is present in  $\text{Tl}_2\text{Ba}_2\text{CuO}_{6+\delta}$ , a single-layer compound with a superconducting transition temperature of  $\sim 90$  kelvin, demonstrating that it is a generic feature of the copper oxide superconductors, independent of the layer sequence. This restricts the theoretical models for the origin of the resonant mode and its role in the mechanism of high-temperature superconductivity.

Electronic conduction in the copper oxide high-temperature superconductors takes place predominantly in structural units of chemical composition  $\text{CuO}_2$ , in which copper and oxygen atoms form an approximately square planar arrangement. Therefore, most theoretical models of high-temperature superconductivity are based on a two-dimensional square lattice. In real materials, however, deviations from this simple situation are nearly always present. For instance, buckling distortions of the  $\text{CuO}_2$  layers found in many copper oxides are thought to have an important influence on the electronic structure and on the superconducting transition temperature  $T_c$ . Interlayer interactions in materials with closely spaced  $\text{CuO}_2$  layers (forming bi- or trilayer units) or additional copper oxide chains in the crystal structure present further complications whose influence on the superconducting properties remains a subject of debate. Experiments on  $\text{Tl}_2\text{Ba}_2\text{CuO}_{6+\delta}$ , a material with unbuckled, widely spaced  $\text{CuO}_2$  layers and a maximum  $T_c$  around 90 K, have played a pivotal role in resolving some issues central to our understanding of these materials (1, 2). We report inelastic neutron-scattering measurements of  $\text{Tl}_2\text{Ba}_2\text{CuO}_{6+\delta}$  near optimum doping

( $T_c \sim 90$  K) that provide evidence of a sharp magnetic resonant mode below  $T_c$ .

A resonant spin excitation of this kind has been extensively characterized by neutron scattering in the bilayer copper oxide  $\text{YBa}_2\text{Cu}_3\text{O}_{6+\delta}$  (3–5) and was recently also observed in  $\text{Bi}_2\text{Sr}_2\text{CaCu}_2\text{O}_{8+\delta}$ , another bilayer compound (6, 7). At all doping levels, strong line shape anomalies of this collective spin excitation below  $T_c$  bear witness to a substantial interaction with charged quasiparticles. Conversely, anomalies in the quasiparticle spectra observed by photoemission (8, 9), optical conductivity (10–13), tunneling (13, 14), and Raman scattering (15) techniques have been interpreted as evidence of coupling to the neutron mode. In the copper oxides [as well as some heavy fermion materials, where similar observations have been made (16)], the correspondence between anomalous features in the spectra of spin and charge excitations has stimulated spin fluctuation-based pairing scenarios (9, 11, 16) that are, however, still controversial (17–19). Other theories of high-temperature superconductivity also rely on the resonant mode (20). Therefore, it is of great interest to establish whether the resonant spin excitation is a general feature of the various crystallographically distinct families of superconducting copper oxides. The failure to detect such an excitation in the single-layer compound  $\text{La}_{2-x}\text{Sr}_x\text{CuO}_{4+\delta}$ , despite much experimental effort (21), has hampered a unified phenomenology of the copper oxides. Also, the prospect that the mode could be a spectral feature specific to bilayer materials has cast a cloud over models in

which spin excitations play a central role. The result of our experiment on single-layer  $\text{Tl}_2\text{Ba}_2\text{CuO}_{6+\delta}$  (whose  $T_c \sim 90$  K is closely similar to that of optimally doped  $\text{YBa}_2\text{Cu}_3\text{O}_{6+\delta}$  and  $\text{Bi}_2\text{Sr}_2\text{CaCu}_2\text{O}_{8+\delta}$ ) implies that strong magnetic interactions between closely spaced  $\text{CuO}_2$  layers are not required for the formation of the resonant mode. The different form of the spin excitation spectrum of  $\text{La}_{2-x}\text{Sr}_x\text{CuO}_{4+\delta}$  may be due to the proximity of a competing instability (22) that could also be responsible for the anomalously low  $T_c \leq 40$  K.

Inelastic magnetic neutron-scattering measurements on conventional triple axis or time-of-flight spectrometers require high-quality copper oxide single crystals with volumes of at least  $1 \text{ cm}^3$ , which are only available for the  $\text{La}_{2-x}\text{Sr}_x\text{CuO}_{4+\delta}$  and  $\text{YBa}_2\text{Cu}_3\text{O}_{6+\delta}$  families. Due to advances in focusing techniques that improve the neutron beam delivery onto small samples, experiments on single crystals of  $\text{Bi}_2\text{Sr}_2\text{CaCu}_2\text{O}_{8+\delta}$  with an order of magnitude smaller volumes have recently become feasible (6, 7). Unfortunately, the crystal growth of the Tl- and Hg-based copper oxide superconductors (which include the only known single-layer compounds with  $T_c$  of order 90 K) has suffered from severe technical difficulties, chief among them the toxicity of some of the constituents. With typical crystal volumes well below  $1 \text{ mm}^3$ , inelastic neutron scattering on these compounds has, thus far, appeared hopeless. We have overcome these difficulties by synthesizing about 300 relatively large ( $0.5$  to  $3 \text{ mm}^3$ ) single crystals of  $\text{Tl}_2\text{Ba}_2\text{CuO}_{6+\delta}$  through a  $\text{CuO}$ -rich flux technique (23) and co-aligning them in a mosaic of total volume  $0.11 \text{ cm}^3$  using Laue x-ray diffraction (Fig. 1A). The crystallographic axes of the individual crystals in the array were aligned with an accuracy of about  $1.5^\circ$  (Fig. 1C). Before alignment, the magnetic susceptibilities of all crystals were measured as a function of temperature (typical data are shown in Fig. 1B). The mean  $T_c$  (onset) of the individual crystals used in the array was  $92.5$  K, with a standard deviation of  $2$  K.

Compared with previous neutron-scattering experiments on much larger crystals of  $\text{Bi}_2\text{Sr}_2\text{CaCu}_2\text{O}_{8+\delta}$ , the background from the Al plates and the adhesive holding the multicrystal array (Fig. 1A) was enhanced, whereas the signal amplitude is substantially smaller due to the single-layer structure. In order to compensate for this reduction in signal-to-background ratio, counting times of up to 5 hours

<sup>1</sup>Max-Planck-Institut für Festkörperforschung, 70569 Stuttgart, Germany. <sup>2</sup>Laboratoire Léon Brillouin, CEA-CNRS, CE Saclay, 91191 Gif sur Yvette, France. <sup>3</sup>CEA Grenoble, Département de Recherche Fondamentale sur la Matière Condensée, 38054 Grenoble cedex 9, France. <sup>4</sup>Institute of Solid State Physics, Russian Academy of Science, Chernogolovka, 142432 Russia.

\*To whom correspondence should be addressed. E-mail: b.keimer@fkf.mpg.de